Monthly Notices
of the
ROYAL ASTRONOMICAL SOCIETY

MNRAS **462,** 2319–2332 (2016)
Advance Access publication 2016 July 19

doi:10.1093/mnras/stw1719

Hektor – an exceptional D-type family among Jovian Trojans

J. Rozehnal,[1,2★] M. Brož,[1] D. Nesvorný,[3] D. D. Durda,[3] K. Walsh,[3]
D. C. Richardson[4] and E. Asphaug[5]

[1]*Institute of Astronomy, Charles University, Prague, V Holešovičkách 2, CZ-18000 Prague 8, Czech Republic*
[2]*Štefánik Observatory, Petřín 205, CZ-11800 Prague, Czech Republic*
[3]*Southwest Research Institute, 1050 Walnut St, Boulder, CO 80302, USA*
[4]*Department of Astronomy, University of Maryland, College Park, MD 20742-2421, USA*
[5]*School of Earth and Space Exploration, Arizona State University, Tempe, AZ 85287, USA*

Accepted 2016 July 14. Received 2016 July 11; in original form 2016 January 6

ABSTRACT

In this work, we analyse Jovian Trojans in the space of suitable resonant elements and we identify clusters of possible collisional origin by two independent methods: the hierarchical clustering and a so-called randombox. Compared to our previous work, we study a twice larger sample. Apart from Eurybates, Ennomos and 1996 RJ families, we have found three more clusters – namely families around asteroids (20961) Arkesilaos, (624) Hektor in the L_4 libration zone and (247341) 2001 UV_{209} in L_5. The families fulfill our stringent criteria, i.e. a high statistical significance, an albedo homogeneity and a steeper size–frequency distribution than that of background. In order to understand their nature, we simulate their long term collisional evolution with the Boulder code and dynamical evolution using a modified SWIFT integrator. Within the framework of our evolutionary model, we were able to constrain the age of the Hektor family to be either 1–4 Gyr or, less likely, 0.1–2.5 Gyr, depending on initial impact geometry. Since (624) Hektor itself seems to be a bilobed-shape body with a satellite, i.e. an exceptional object, we address its association with the D-type family and we demonstrate that the moon and family could be created during a single impact event. We simulated the cratering event using a smoothed particle hydrodynamics. This is also the first case of a family associated with a D-type parent body.

Key words: celestial mechanics.

1 INTRODUCTION

Jovian Trojans are actually large populations of minor bodies in the 1:1 mean motion resonance with Jupiter, librating around L_4 and L_5 Lagrangian points. In general, there are two classes of theories explaining their origin: (i) a theory in the framework of accretion model (e.g. Goldreich, Lithwick & Sari 2004; Lyra et al. 2009) and (ii) a capture of bodies located in libration zones during a migration of giant planets (Morbidelli et al. 2005; Morbidelli et al. 2010; Nesvorný, Vokrouhlický & Morbidelli 2013), which is preferred in our Solar system. Since the librating regions are very stable in the current configuration of planets and they are surrounded by strongly chaotic separatrices, bodies from other source regions (e.g. Main belt, Centaurs, Jupiter family comets) cannot otherwise enter the libration zones and Jupiter Trojans thus represent a rather primitive and isolated population.

Several recent analyses confirmed the presence of several families among Trojans (e.g. Nesvorný, Brož & Carruba 2015; Vinogradova 2015). The Trojan region as such is very favourable for dynamical studies of asteroid families, because there is no significant systematic Yarkovsky drift in semimajor axis due to the resonant dynamics. On the other hand, we have to be aware of boundaries of the libration zone, because ballistic transport can cause a partial depletion of family members. At the same time, as we have already shown in Brož & Rozehnal (2011), no family can survive either late phases of a slow migration of Jupiter, or Jupiter 'jump', that results from relevant scenarios of the Nice model (Morbidelli et al. 2010). We thus focus on post-migration phase in this paper.

We feel the need to evaluate again our previous conclusions on even larger data sets, that should also allow us to reveal as-of-yet unknown structures in the space of proper elements or unveil possible relations between orbital and physical properties (e.g. albedos, colours, diameters) of Jovian Trojans.

In Section 2, we use new observational data to compute appropriate resonant elements. In Section 3, we use albedos obtained by Grav et al. (2012) to derive size–frequency distributions (SFDs) and

★ E-mail: rozehnal@observatory.cz

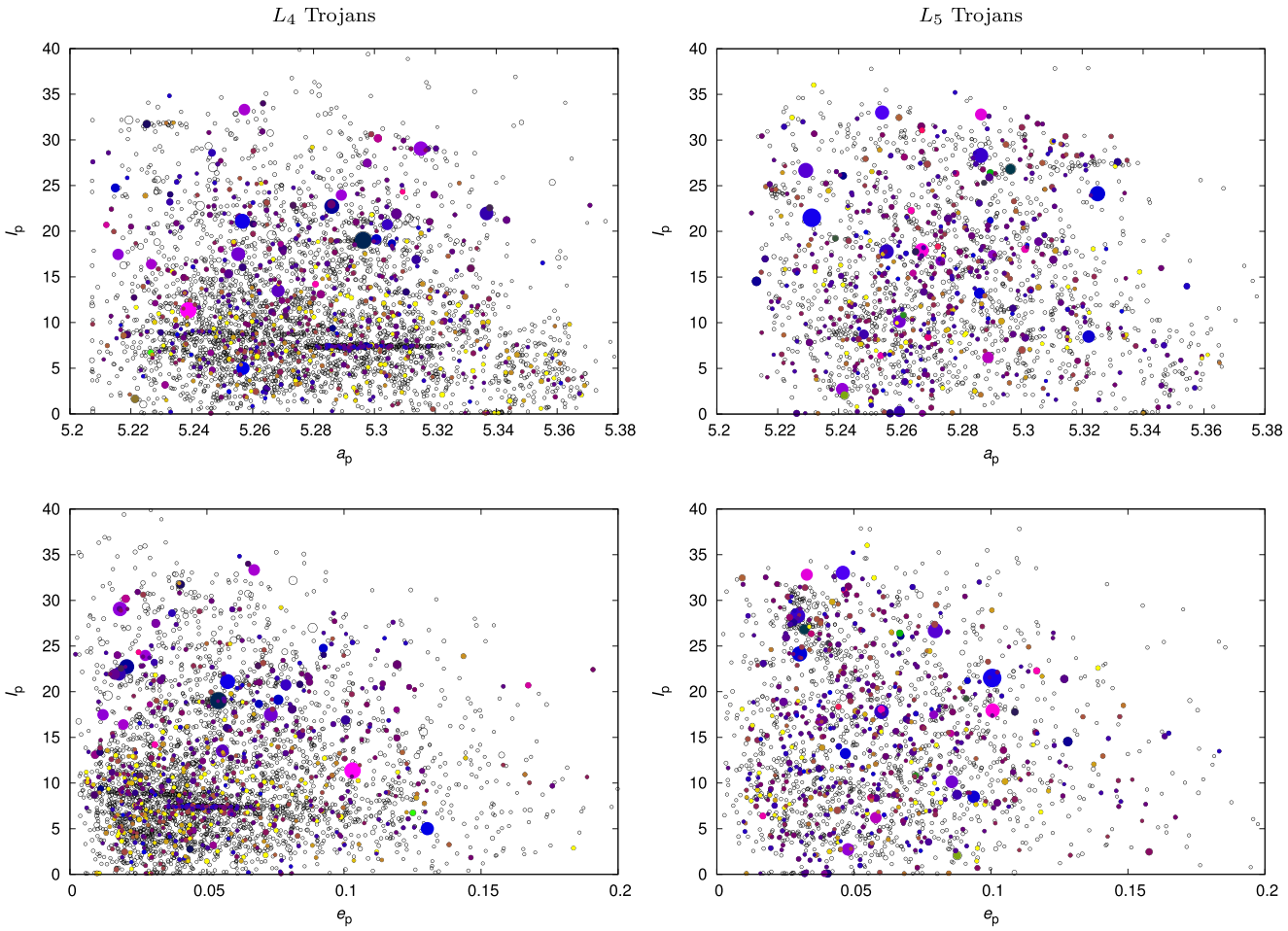

Figure 1. The resonant semimajor axis versus inclination (a_p, I_p) (top) and eccentricity versus inclination (e_p, I_p) (bottom) for L_4 (left) and L_5 Trojans (right). The circles indicate relative diameters of bodies, as determined by *WISE* (Grav et al. 2011), or when unavailable, computed from the absolute magnitude H and geometric albedo p_V, which we assumed to be $p_V = 0.07$ for both the L_4 and L_5 Trojans (*WISE* median value is $p_V = 0.072$ for L_4 and $p_V = 0.069$ for L_5 Trojans). Colours correspond to the values of p_V, blue are dark ($p_V \simeq 0.05$) and yellow are bright ($p_V \simeq 0.25$). One can see clearly all asteroid families on this plot, especially in (a_p, I_p), because they tend to be confined in inclinations.

distribution of albedos, which seem to be slightly dependent on the proper inclination I_p. In Section 4, we identify families among Trojans with our new 'randombox' method. We discuss properties of statistically significant families in Section 5. Then we focus mainly on the Hektor family because of its unique D-type taxonomical classification, which is the first of its kind. We also discuss its long-term dynamical evolution. In Section 6, we simulate collisional evolution of Trojans and we estimate the number of observable families among Trojans. Finally, in Section 7, we simulate an origin of the Hektor family using smoothed particle hydrodynamics (SPH) and we compare results for single and bilobed targets. Section 8 is devoted to Conclusions.

2 NEW OBSERVATIONAL DATA

2.1 Resonant elements

We computed resonant elements, i.e. the averaged semimajor axis $\bar{a}$, libration amplitude Δa_p, eccentricity e_p and inclination I_p of 3907 Trojans in L_4 cloud and 1945 Trojans in L_5 cloud. As an input, we used osculating elements listed in AstOrb catalogue (Bowell et al. 2002), released in 2014 July. A detailed description of the resonant elements computation can be found in Brož & Rozehnal (2011). Positions of Trojans in the space of proper elements (a_p, I_p), where $a_p = \bar{a} + \Delta a_p$, and ($e_p$, I_p), calculated with a suitably modified version of the SWIFT integrator (Levison & Duncan 1994), are presented graphically in Fig. 1, together with their sizes and albedos.[1]

2.2 *WISE* and AKARI albedos and diameters

To construct SFDs of the whole L_4 and L_5 Trojan populations and later of individual families, we mostly used *WISE* albedos and diameters derived by Grav et al. (2012). We also compared the respective values to AKARI, as reported by Usui et al. (2011).[2]

We used albedo values of 1609 Trojans in both L_4 and L_5 clouds obtained by *WISE*; about one-third of these albedos were obtained during cryo-phase, the rest were measured in post-cryo-phase (see Grav et al. 2011).

[1] The table of resonant elements is listed online at http://sirrah.troja.mff.cuni.cz/~mira/mp/trojans/.

[2] While there are some differences between individual values even at 3σ level, they do not seem to be important for population studies like ours.

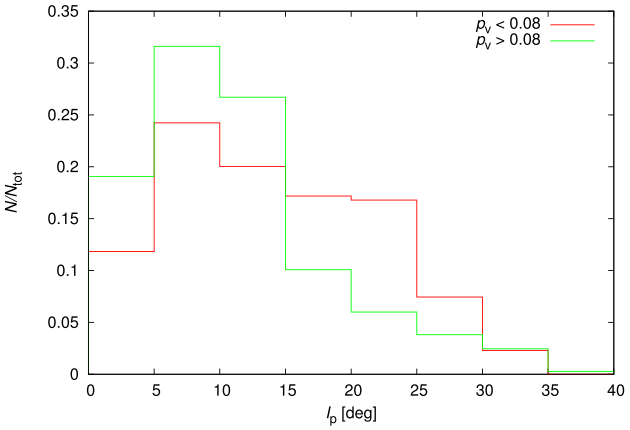

Figure 2. The differential histogram of the resonant inclination I_p for L_4 Trojans with a lower albedo ($p_V < 0.08$, red) and a higher one ($p_V > 0.08$, green). Eurybates family was removed from the data set.

3 PHYSICAL CHARACTERIZATION OF TROJAN POPULATIONS

3.1 Albedo distribution and taxonomy

The values of visible albedos p_V of Trojans derived by Grav et al. (2012) vary in the range from $p_V = 0.025$ to $\simeq 0.2$. Distributions of albedos are qualitatively the same for both L_4 and L_5 populations. The median albedo of *WISE* sample is $\widetilde{p}_v = 0.072 \pm 0.017$ for L_4 and $\widetilde{p}_v = 0.069 \pm 0.015$ for L_5. These values of visible albedos mostly correspond to C or D taxonomical classes in Tholen taxonomic classification scheme (Mainzer et al. 2011). However, there is a significant presence of small asteroids ($D < 15$ km) with apparently high albedo – almost 20 per cent of asteroids in L_4 and 13 per cent of asteroids in L_5 have albedo $p_V > 0.10$. As stated in Grav et al. (2012), this is probably not a physical phenomenon, it is rather due to the fact that for small diameters, the photon noise contribution becomes too significant.

When we compute the median albedo from AKARI data, we realize that its value is slightly lower ($\widetilde{p}_v = 0.054 \pm 0.005$) than that from *WISE*, but when we compute the median from *WISE* values for the same asteroids which are listed in AKARI catalogue, we obtain a similar value ($\widetilde{p}_v = 0.061 \pm 0.012$). What is more serious, AKARI and WISE *data* differ considerably for large asteroids with $D > 100$ km – the average difference between albedos is $|p_{V_{AKARI}} - p_{V_{WISE}}| = 0.02$. The same difference we see in derived diameters. These discrepancies may be caused, for example, by limitations of the thermal model (cf. spheres in NEATM models). Hereinafter, we prefer to use the *WISE* data when available, because they represent orders of magnitude larger sample than AKARI.

When we split Trojan asteroids according to their albedo into two rather artificial subpopulations with $p_V < 0.08$ and $p_V > 0.08$, respectively, and then we compute distributions of these subpopulations with respect to the resonant inclination I_p, we get two different pictures. As can be seen in Fig. 2, most bodies have resonant inclinations $I_p < 15^\circ$, but there are 77 per cent of bodies with higher albedo with $I_p < 15^\circ$, while only 55 per cent of the population with lower albedo is located in the same range of inclinations. This is a similar phenomenon as described by Vinogradova (2015), who reported different upper limits in inclinations for different taxonomical types obtained mostly from SDSS colour data.

3.2 Size–frequency distributions

The *WISE* data (Grav et al. 2011, 2012) provide very useful source of information on diameters we need to construct SFDs of Trojan populations in L_4 and L_5. However, the sample measured by *WISE* is not complete. In our previous work (Brož & Rozehnal 2011), we constructed the SFDs assuming a constant albedo which we set to be equal to the median albedo of Trojans that was measured back then. Since the number of measurements was very low (several tens), this was the only reasonable way. Now we choose another method to construct more reliable SFDs. As we calculated resonant elements for more than 5800 Trojans and we have more than one quarter of appropriate albedos, we constructed the SFDs by assigning albedos randomly from the observed *WISE* distribution to the remaining Trojans, whose albedo was not measured. To avoid a bias, we compared different SFDs constructed with different random generator seeds and we realized that the overall shape of SFDs does not change noticeably, the slope γ varies in the range of ± 0.1 at most. The SFDs we constructed this way are shown in Fig. 3.

The SFDs for the L_4 and L_5 clouds look slightly different, especially in the size range from 60 to 100 km. This part of the SFD is not influenced by the Eurybates family, the largest family among Trojans, because all its members have diameters $D < 50$ km. We used these SFDs to determine the ratio of the number of asteroids in L_4 and L_5 clouds. There are 2746 asteroids with diameter $D > 8$ km in L_4 and 1518 asteroids in L_5. When we remove all family members with diameters $D > 8$ km, we have 2436 asteroids in L_4 and 1399 in L_5. However, this sample may be still influenced by debris produced by catastrophic disruptions of small bodies ($D \geq 50$ km), which need not to be seen as families. Counting only asteroids with diameter $D > 20$ km, which corresponds to the absolute magnitude $H \simeq 12$, and removing family members, we get the ratio $N_{L_4}/N_{L_5} = 1.3 \pm 0.1$. As this is entirely consistent with value of Nesvorný et al. (2013), which was derived for Trojans with $H > 12$, and with Grav et al. (2012), whose estimate is $N_{L_4}/N_{L_5} = 1.4 \pm 0.2$, we can confirm a persisting asymmetry between the number of L_4 and L_5 Trojans in new data. Although for bodies with diameter $D > 100$ km, the L_5 cloud has more asteroids than L_4, the total number of these bodies is of the order of 10, so this is just an effect of small-number statistics and does not affect the N_{L_4}/N_{L_5} ratio much.

4 FAMILIES DETECTION METHODS

A brief inspection of the resonant-element space (a_p, e_p, I_p) (see Fig. 1), reveals several locations with higher concentrations of bodies. These could be collisional families, created by a disruption of a parent body during a random collision, but they could also originate randomly by chaotic diffusion and due to effects of secular and high-order resonances. To be regarded as a family, the cluster must comply with, inter alia, the following criteria: (i) it must be concentrated in the space of proper elements; (ii) the cluster must have the SFD different from that of the whole L_4 and L_5 population; (iii) the last criterion is usually spectral, or at least, albedo homogeneity of family members, but so far, there are not enough sufficiently accurate data for Trojans, especially for bodies with diameters $D < 50$ km, which usually form a substantial part of Trojan families. Therefore, we cannot perform any detailed spectral analysis in this work.

We analysed the space of resonant elements both in terms of mutual distances among bodies and in terms of statistical probability that clusters are not random.

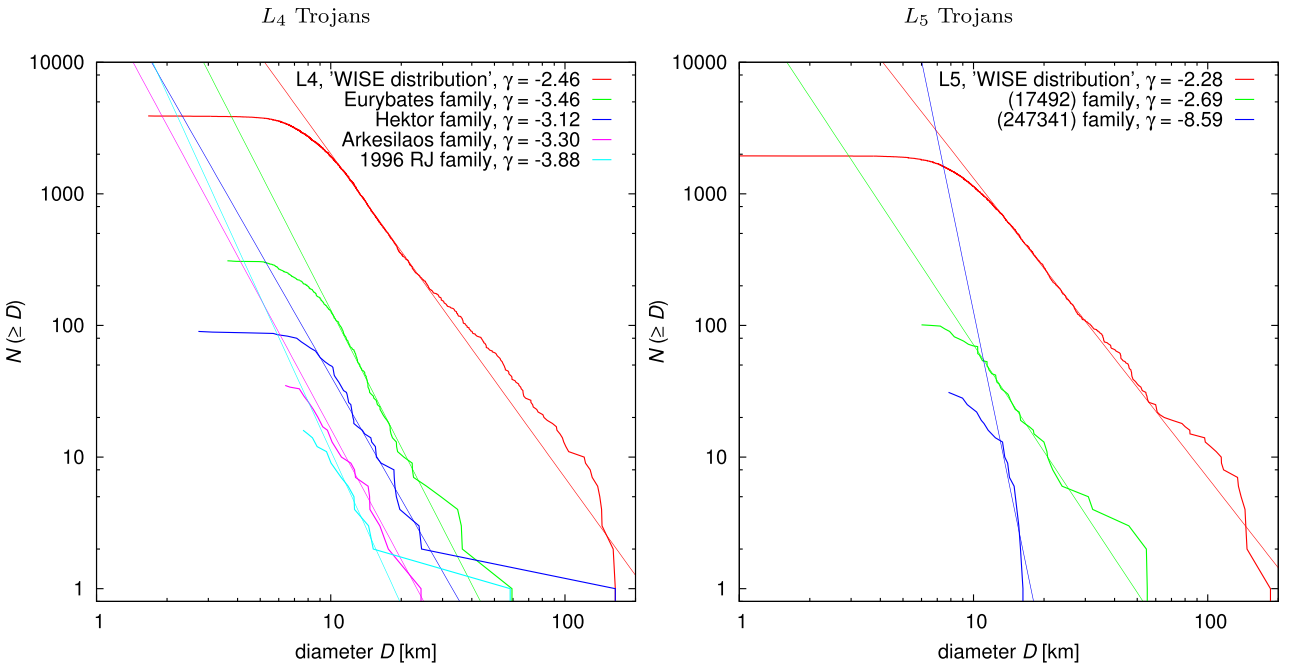

Figure 3. Size–frequency distributions for both L_4 and L_5 Trojans, constructed using the albedos measured by *WISE* satellite (Grav et al. 2012). Since *WISE* data cover just about 18 per cent of L_4 and 29 per cent of L_5 Trojans known today, we assigned albedos randomly from the *WISE* distribution to the remaining Trojans. We also present SFDs of individual asteroid families discussed in the main text. There are also our fits of each SFD in the range $D = 12$–30 km by the power law $N(>D) = CD^{\gamma}$. As we can see, both clouds seem to be near the collisional equilibrium ($\gamma \simeq -2.5$; Dohnanyi 1969), while most families have slope γ significantly steeper. Of course, we can expect the slopes of the SFDs become shallower for smaller D due to observational incompleteness.

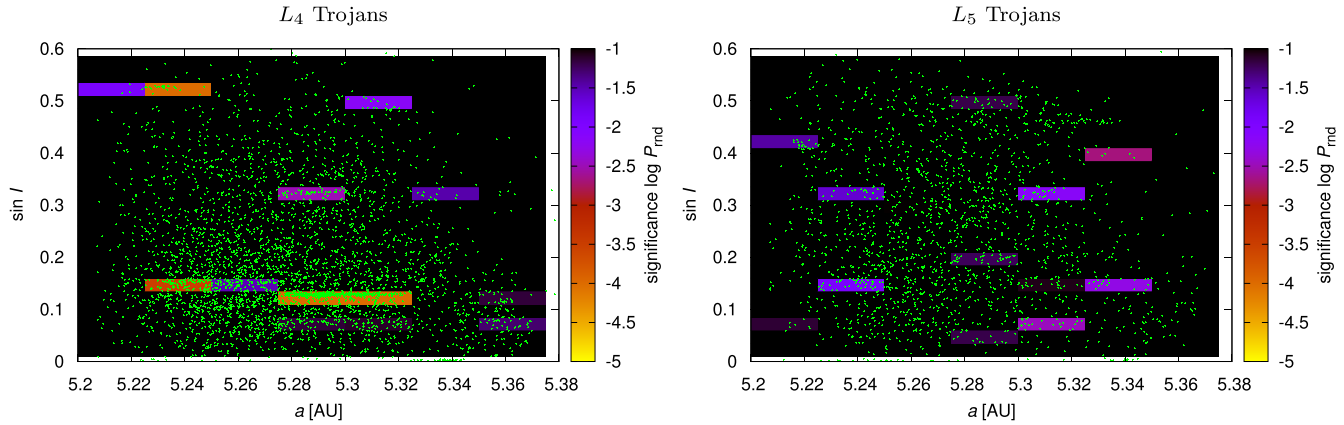

Figure 4. The statistical significance p expressed as colour on the logarithmic scale for observed asteroids in the proper semimajor axis versus proper inclination plane (a_p, $\sin I_p$) (i.e. the same data as in Fig. 1). L_4 Trojans are on the left, L_5 Trojans on the right. We computed the values of p for seven times in 18 boxes using our 'randombox' method. The range in proper eccentricity is 0.00–0.20. Statistically significant groups appear as orange boxes and they correspond to the families reported in Table 1.

4.1 Randombox method

Besides the commonly used hierarchical clustering method (HCM; Zappalà et al. 1994), we applied a 'randombox' method, based on numerical Monte Carlo (MC) simulations. This method allows us to compute the statistical significance of the clusters, i.e. the probability that the cluster is a random concentration of bodies in the space of proper elements (a_p, e_p, $\sin I_p$).

We divided the space of proper elements into equally sized 'boxes' with dimensions $\Delta a_p = 0.025$ au, $\Delta e_p = 0.2$ and $\Delta \sin I_p = 0.025$. Then we created $N = 100\,000$ random distributions of the same number of bodies which are observed together in the given box and two adjacent boxes (in the direction of the y-axis, cf. Fig. 4), and we counted number of positive trials N^+, for which the randomly generated number of bodies in the central box was larger than the observed one. From here, we can calculate the probability P_{rnd}, that the observed number of bodies in the box is random: $P_{rnd} = N^+/N$.

Alternatively, one can also use our analytical formula:

$$p_{rnd} = \frac{\sum_{k=n_2}^{n} C(n,k)V'(n_{box}-1, n-k)}{V'(n_{box}, n)}, \quad (1)$$

where n denotes the total number of bodies, n_{box} is the total number of boxes (three in our case), n_2 is the observed number of bodies in the middle box, k is the number of observed bodies in the current

Table 1. Physical properties of Trojan families identified by both the 'randombox' and the HCM methods. We list family identification number (FIN; as in Nesvorný et al. 2015), the designation of the family, the designation of the asteroid with which the family is associated (i.e. usually the largest remnant of the parent body), the cut-off velocity $v_{\rm cutoff}$, for which family is still clearly detached from the background, and the number of members of the family $N_{\rm memb}$ corresponding to the respective $v_{\rm cutoff}$. Next, we list optical albedos $p_{\rm V}$ of associated bodies determined by Grav et al. (2012) from *WISE* observations, and their taxonomical classification.

FIN	Family designation	Cloud	Asteroid designation	$v_{\rm cutoff}$(m s^{-1})	$N_{\rm memb}$	$p_{\rm V}$(*WISE*)	Tax. type
004	Hektor	L_4	(624) Hektor	110	90	0.087 ± 0.016	D
005	Eurybates	L_4	(3548) Eurybates	60	310	0.060 ± 0.016	C/P
006	1996 RJ	L_4	(9799) 1996 RJ	140	17	0.082 ± 0.014	–
008	Arkesilaos	L_4	(20961) Arkesilaos	55	35	n/a	–
009	Ennomos	L_5	(17492) Hippasos	100	104	0.064 ± 0.012	–
010	2001 UV_{209}	L_5	(247341) 2001 UV_{209}	120	30	0.088 ± 0.023	–

box, $C(n, k)$ are combinations without repetitions, i.e. the total number of trials to select k bodies observed in the current box from the total number of n bodies; $V'(n_{\rm box} - 1, n - k)$ are variations with repetitions, i.e. the total number of trials to distribute the remaining bodies into the remaining boxes; and $V'(n_{\rm box}, n)$ are also variations with repetitions, i.e. the total number of trials to distribute all n bodies into all $n_{\rm box}$ boxes. We verified the results of the analytical formula (1) by the MC method.

We plot the results in Fig. 4 for both the L_4 and L_5 clouds. In comparison with Fig. 1, one can see that for all clusters we identified as families the probability $P_{\rm rnd}$ varies between $2 \cdot 10^{-3}$ and $5 \cdot 10^{-5}$, i.e. the probability that clusters are random fluctuations is indeed very low.

We also re-evaluated all families identified by the HCM using the 'randombox' method, which makes our decision whether the cluster is a real family much more quantitative.

4.2 Hierarchical clustering method

We also used the HCM independently to extract significant clusters. Families identified by both the 'randombox' and HCM methods are listed in Table 1. For each family, we constructed a dependence of the number of members of the cluster $N_{\rm memb}$ on the cut-off velocity $v_{\rm cutoff}$. Because the number of members of a real collisional family rises first slowly with rising $v_{\rm cutoff}$ (Brož & Rozehnal 2011) – in contrast with random clusters which are merging very quickly with the background – the constructed dependence allows us to guess a realistic number of family members $N_{\rm memb}$. For all families listed in Table 1, we were convinced that they fulfill this criterion. However, we cannot distinguish possible interlopers this way, and it is also possible that some fraction of family members with high $v_{\rm cutoff}$ (so called halo, as in Brož & Morbidelli 2013) remains unidentified in the surrounding background.

5 PROPERTIES OF STATISTICALLY SIGNIFICANT FAMILIES

5.1 Eurybates

As we have already demonstrated in Brož & Rozehnal (2011), the family associated with asteroid (3548) Eurybates is the largest collisional family, and it is the only family among Trojans with the parent body size $D_{\rm PB} > 100$ km, which originated by a catastrophic disruption (this means that the mass ratio of the largest remnant to the parent body $M_{\rm LR}/M_{\rm PB} < 0.5$).

Using new albedos derived by Grav et al. (2012), we recalculated the overall SFD slope of the family to be $\gamma = -3.4 \pm 0.1$. As the *WISE* sample provides albedos for only about one-fifth of the family members, we calculated two values of γ: the first one assuming that remaining asteroids have a constant albedo $p_{\rm V} = 0.06$, the second one by assigning albedos randomly from the *WISE* distribution, as described in Section 3.2. Both values are equal within their errorbars. The new slope γ is significantly steeper than our previous calculation ($\gamma = -2.5 \pm 0.1$), derived with the assumption of a constant albedo of all members of the family. The lower value was most likely caused by a significant observational incompleteness in the size range from $D = 12$–30 km.

We also derived the new value of the parent body diameter, which is still above the limit of 100 km. An extrapolation of the SFD by a power law gives the value $D_{\rm PB} \simeq 140$ km. By fitting the synthetic SFDs from SPH simulations (Durda et al. 2007), we obtained the value $D_{\rm PB(SPH)} \simeq 155$ km.

5.2 Hektor – the first D-type family

Since asteroid (624) Hektor is a close binary with a satellite (Marchis et al. 2014), i.e. an exceptional object, we want to address its association with the family. The cluster around the largest Trojan asteroid appears in the space of proper elements as a relatively compact group, which is limited particularly in proper inclinations, $I_{\rm p} \in \langle 18\overset{\circ}{.}13;\ 19\overset{\circ}{.}77\rangle$, and with resonant semimajor axes located in the interval $a_{\rm p} \in \langle 5.234;\ 5.336\rangle$ au. The number of members of this group slowly increases with increasing cut-off velocity up to $v_{\rm cutoff} \simeq 110$ m s^{-1}, above which it quickly joins the background. With our randombox method, we estimated the probability that the family is just a random fluke to be as low as $P_{\rm rnd} \simeq 2 \cdot 10^{-3}$.

The nominal diameter of asteroid (624) Hektor derived from its albedo is 164 km (Grav et al. 2012), but the albedo measured by AKARI $p_{\rm V} = 0.034 \pm 0.001$ (Usui et al. 2011) totally differs from that measured by *WISE*, $p_{\rm V} = 0.087 \pm 0.016$. and these values do not match even within the error limits. This may be caused by applying a thermal model assuming spheres to the bilobed shape of the asteroid (Marchis et al. 2014). We hence do not determine Hektor's diameter from its albedo, but from fits of Marchis et al. (2014), which effective value $D = (250 \pm 26)$ km is suitable within its uncertainty for all possible geometries (convex, bilobe and binary). For other bodies in family, we use a nominal value $p_{\rm V} = 0.072$, which is the median of *WISE* measurements.

Asteroid (624) Hektor is often classified as D-type (e.g. Cruikshank et al. 2001; Emery, Cruikshank & Van Cleve 2006; Emery, Burr & Cruikshank 2011). We tried to evaluate taxonomical classification of other family members and we have found colours for two more expected family members in SDSS-MOC vers. 4 (Ivezić et al. 2002): asteroids (65000) 2002 AV63 and (163702) 2003 FR72. Even though the photometric noise in individual bands is not negligible ($\sigma_i = 0.02$ mag up to $\sigma_u = 0.12$ mag), both of them

are D-types, with principal components (also known as slopes) $PC_1 > 0.3$. This seems to support the D-type classification of the whole family.

We also tried to constrain the taxonomic classification of the family members by comparing their infrared (IR) albedos p_{IR} and visual albedos p_V as described in Mainzer et al. (2011), but there are no data for family members in the *W1* or *W2* band of the *WISE* sample, which are dominated by reflected radiation.

The fact that we observe a collisional family associated with a D-type asteroid is the main reason we use word 'exceptional' in connection with the Hektor family. As we claimed in Brož et al. (2013), in all regions containing a mixture of C-type and D-type asteroids (e.g. Trojans, Hildas, Cybeles), there have been only C-type families observed so far, which could indicate that disruptions of D-type asteroids leave no family behind, as suggested by Levison et al. (2009). Nevertheless, our classification of the Hektor family as D-type is not in direct contradiction with this conclusion, because Levison et al. (2009) were concerned with catastrophic disruptions, while we conclude below that the Hektor family originated from a cratering event, i.e. by an impactor with kinetic energy too small to disrupt the parent body.

5.2.1 *Simulations of long-term dynamical evolution*

To get an upper limit of the age of the Hektor family, we simulated a long-term evolution of seven synthetic families created for different breakup geometries. Our model included four giant planets on current orbits, integrated by the symplectic integrator SWIFT (Levison & Duncan 1994), modified according to Laskar & Robutel (2001), with the timestep of $\Delta t = 91$ d and timespan 4 Gyr.

We also accounted for the Yarkovsky effect in our simulations. Although in a first-order theory, it is not effective in zero-order resonances (it could just shift libration centre, but there is no systematic drift in semimajor axis) and the observed evolution of proper elements is mainly due to chaotic diffusion, in higher order theories, the Yarkovsky effect can play some role. In our model, we assumed a random distribution of spins and rotation periods (typically several hours), the bulk and surface density $\rho_{bulk} = \rho_{surf} = 1.3\ \mathrm{g\,cm^{-3}}$, the thermal conductivity $K = 0.01\ \mathrm{W\,m^{-1}\,K^{-1}}$, the specific heat capacity $C = 680\ \mathrm{J\,kg^{-1}\,K^{-1}}$, the Bond albedo $A_B = 0.02$ and the IR emissivity $\epsilon = 0.95$.

We created each synthetic family by assigning random velocities to 234 bodies (i.e. three times more than the number of the observed family members), assuming an isotropic velocity field with a typical velocity of 70 $\mathrm{m\,s^{-1}}$, corresponding to the escape velocity from parent body (Farinella, Froeschlé & Gonczi 1994). Here we assumed the velocity of fragments to be size independent. Possible trends in the ejection velocity field cannot be easily revealed in the (a, H) space in the case of the Hektor family, because of its origin by a cratering event – there is a large gap in the range between absolute magnitude of (624) Hektor ($H = 7.20$) and other bodies ($H > 11.9$), so we are not able to distinguish a simple Gaussian dispersion from the physical dependence (cf. Carruba & Nesvorný 2016). Either way, we are interested in the orbital distribution of mostly small bodies. Our assumption of size-independent ejection velocity is also in good agreement with results of SPH models (see subsection 7.3 and Fig. 13).

To create a synthetic family in the same position as occupied by the observed Hektor family, we integrated the orbit of asteroid (624) Hektor with osculating elements taken from AstOrb catalogue (Bowell et al. 2002), until we got appropriate values of the true anomaly f and the argument of pericentre ω. We tried values of f ranging from 0° to 180° with the step of 30° and ω always satisfying the condition $f + \omega = 60°$, i.e. we fixed the angular distance from the node to ensure a comparably large perturbations in inclinations.

Initial positions of synthetic families members just after the disruption, compared to the observed Hektor family, are shown in Fig. 5. To make a quantitative comparison of the distribution in the space of proper elements, we used a two-dimensional Kolmogorov–Smirnov (KS) test to compute KS distance of the synthetic family to the observed one with the output timestep of 1 Myr. The results for different initial geometries are shown in Fig. 6.

Our two best fits corresponding to the lowest KS distance are displayed in Fig. 7. As we can see from the image of the whole Trojan L4 population, Hektor seems to be near the outskirts of the librating region (cf. Fig. 1). In Fig. 5, we can note that there are almost no observed asteroids in the shaded area with $a_p > 5.32$ au, but we can see some synthetic family members in the left-hand panel of Fig. 7 (initial geometry $f = 0°$, $\omega = 60°$).

On the other hand, when we look at right-hand panel of Fig. 7 (initial geometry $f = 150°$, $\omega = 270°$), we can see that there are many fewer bodies in the proximity of the border of the stable librating region. One can also see the initial 'fibre-like' structure is still visible on the left, but is almost dispersed on the right.

Hence, we conclude that the geometry at which the disruption occurred is rather $f = 150°$, $\omega = 270°$ and the corresponding age is between 1 and 4 Gyr. The second but less likely possibility is that the disruption could have occurred more recently (0.1–2.5 Gyr) at $f = 0°$, $\omega = 60°$.

5.2.2 *Parent body size from SPH simulations*

We tried to estimate the parent body size of Hektor family and other families by the method described in Durda et al. (2007). To this point, we calculated a pseudo$-\chi^2$ for the whole set of synthetic SFDs as given by the SPH simulations results (see Fig. 8).

Parent body sizes $D_{PB(SPH)}$ and mass ratios of the largest fragment and parent body M_{LF}/M_{PB} estimated by this method are listed in Table 2. The parent body size for Hektor family we derived from SPH simulations is $D_{PB(SPH)} = (260 \pm 10)$ km, the impactor diameter $D_{imp} = (24 \pm 2)$ km, the impactor velocity $v_{imp} = (4 \pm 1)\ \mathrm{km\,s^{-1}}$ and the impact angle $\varphi_{imp} = (60° \pm 15°)$. We will use these values as initial conditions for simulations of collisional evolution below.

5.3 1996 RJ – extremely compact family

In our previous work, we mentioned a small cluster associated with asteroid (9799) 1996 RJ, which consisted of just nine bodies. With the contemporary sample of resonant elements, we can confirm that this cluster is indeed visible. It is composed of 18 bodies situated near the edge of the librating zone on high inclinations, within the ranges $I_p \in \langle 31.^\circ 38;\ 32.^\circ 27\rangle$ and $a_p \in \langle 5.225\,;5.238\rangle$ au. As it is detached from the background in the space of proper elements, it remains isolated even at high cut-off velocity $v_{cutoff} = 160\ \mathrm{m\,s^{-1}}$.

Unfortunately, we have albedos measured by *WISE* for just four members of this family. These albedos are not much dispersed. They range from $p_V = 0.079 \pm 0.019$ to 0.109 ± 0.029 and, compared to the median albedo of the whole L_4 population $\widetilde{p_V} = 0.072 \pm 0.017$, they seem to be a bit brighter, but this statement is a bit inconclusive.

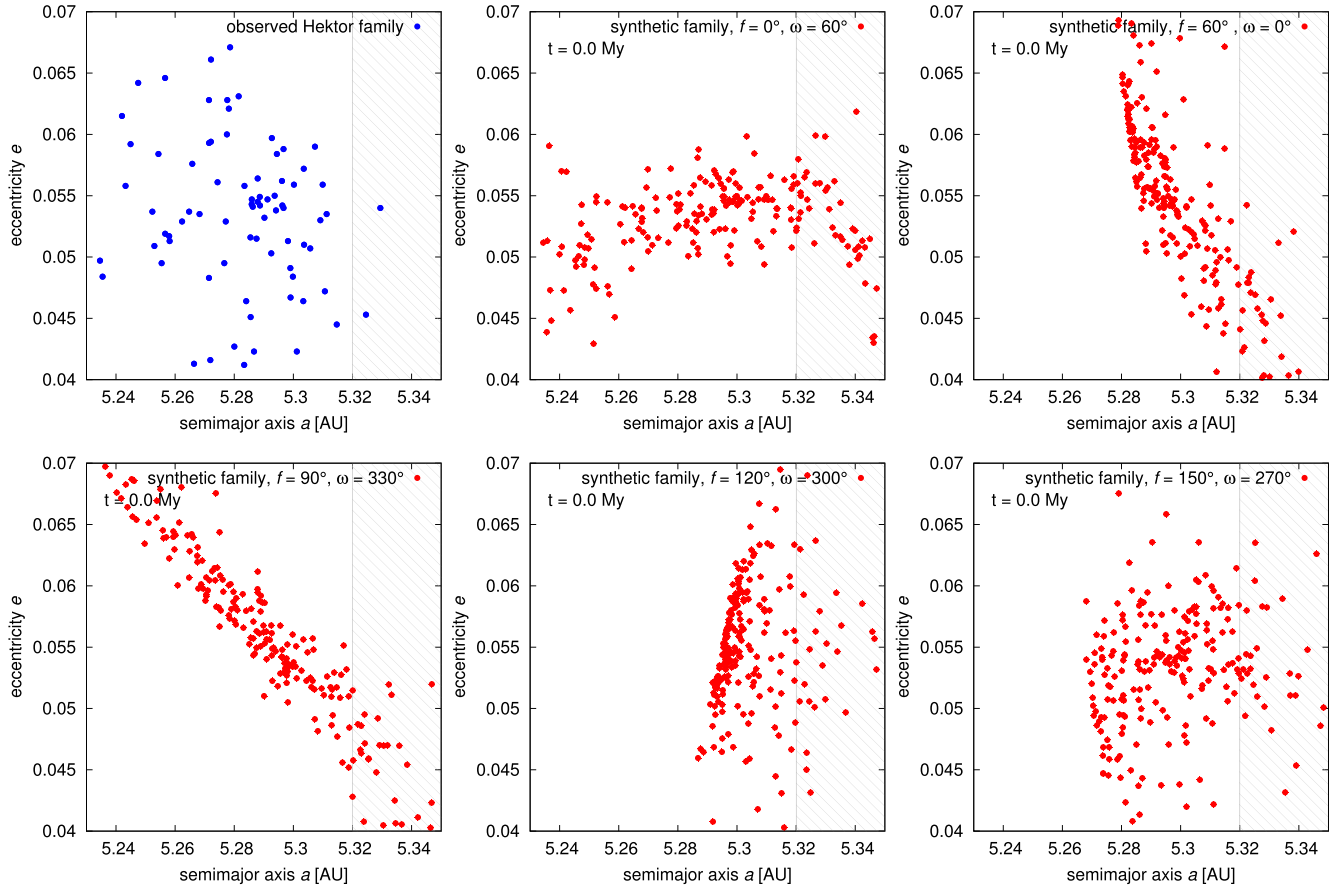

Figure 5. Initial conditions for simulations of long-term evolution of synthetic families (red), compared to the observed Hektor family (blue) in the space of proper elements (a_p, e_p). Each figure shows a different disruption geometry with different values of the true anomaly f and the argument of pericentre ω. Note the shaded area in the top-left figure – there are only two observed asteroids with proper semimajor axis $a_p > 5.32$ au. This is due to the proximity to the border of the stable librating region. As there are many more synthetic asteroids in this region in all cases of initial distributions, we need to simulate a dynamical evolution of the family.

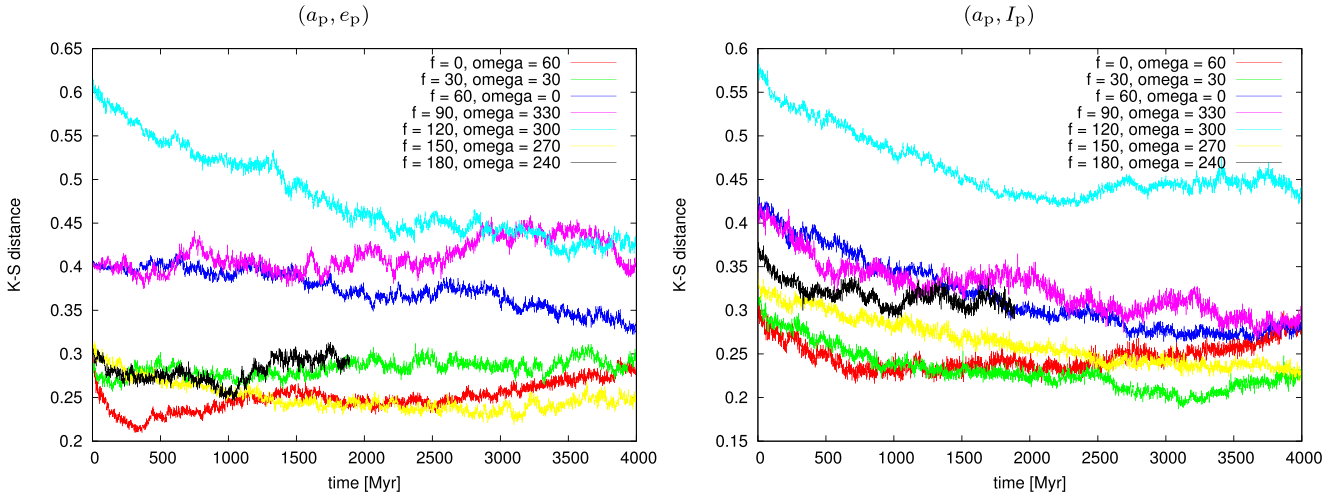

Figure 6. Kolmogorov–Smirnov distance D_{KS} versus time for seven different synthetic families compared with the observed Hektor family. Two-dimensional KS test was computed for the distributions of synthetic and observed families in the space of proper elements (a_p, e_p) (left) and (a_p, I_p) (right). The synthetic families were created assuming different impact geometries, namely the true anomaly $f = 0°$, 30°, 60°, 90°, 120°, 150°, 180° and the argument of pericentre $\omega = 60°$, 30°, 0°, 330°, 300°, 270°, 240°, which were combined so that the sum $f + \omega = 60°$. The averaged distance D_{KS} changes in the course of dynamical evolution and we can see two minima: for $f = 0°$ and $\omega = 60°$ (red curve), it is at about (350 ± 100) Myr; for $f = 150°$ and $\omega = 270°$ (yellow curve), there is a flat minimum at (2800 ± 1500) Myr. Since the red and yellow curves are overlapping in the range from 1800 to 2500 Myr, we adopt the values of possible ages as 100–2500 Myr for the $f = 0°$ and $\omega = 60°$ geometry (red curve) and 1000–4000 Myr for the $f = 150°$ and $\omega = 270°$ geometry (yellow curve).

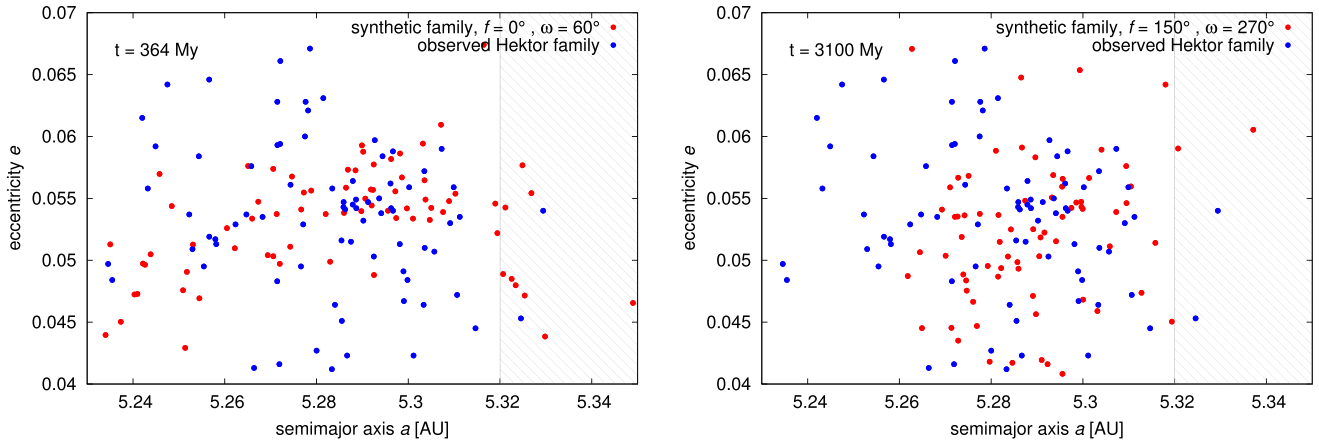

Figure 7. Two evolved synthetic families in the space of proper elements (a_p, e_p), which correspond to the minima of KS distance in Fig. 6. Left-hand picture shows the synthetic family (red) with $f = 0°$ and $\omega = 60°$ after 364 Myr of evolution in comparison with the observed Hektor family (blue). Right-hand picture corresponds to the synthetic family with $f = 150°$ and $\omega = 270°$ after 3100 Myr of evolution. These two pictures differ in fine details, which cannot be accounted for in the KS statistics: (i) the 'fibre-like' structure of the relatively young family is still visible in the left-hand picture; (ii) there are many fewer synthetic bodies in the shaded area of the right picture ($a_p > 5.32$ au) than on the left, which is closer to the observed reality.

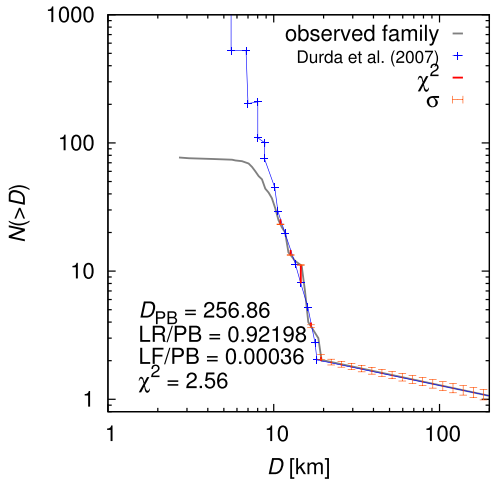

Figure 8. Our best-fitting size–frequency distribution of Hektor family by scaled SFDs from SPH simulations of Durda et al. (2007). In this particular case, $D_{PB(SPH)} = 257$ km, impactor diameter $D_{imp} = 48$ km, impactor velocity $v_{imp} = 4\,km\,s^{-1}$ and impact angle $\varphi_{imp} = 60°$. However, other fits with similar pseudo-χ^2 suggest the uncertainties are as follows: $\Delta D_{PB(SPH)} = 10$ km, $\Delta D_{imp} = 2$ km, $\Delta v_{imp} = 1\,km\,s^{-1}$ and $\Delta\varphi_{imp} = 15°$. SFD shape seems to be more dependent on impact geometry than on impact velocity.

5.4 Arkesilaos

This family is located on low inclinations $I_p \in \langle 8.52°; 9.20°\rangle$, in the range of $a_p \in \langle 5.230; 5.304\rangle$ au. It is clearly visible in the space of proper elements, although this area of L_4 cloud is very dense.

Still, it is difficult to find the largest remnant of the parent body, because this region is populated mainly by small asteroids with absolute magnitudes $H > 12$. The only four asteroids with $H < 12$ are (2148) Epeios with $H = 10.7$, (19725) 1999 WT_4 with $H = 10.7$, (38600) 1999 XR_{213} with $H = 11.7$ and (20961) Arkesilaos with $H = 11.8$. The only diameter derived from measured albedo is that of (2148) Epeios, which is $D = (39.02 \pm 0.65)$ km. Diameters of remaining bodies were calculated from their absolute magnitude assuming albedo $p_V = 0.072$, which is the median of L_4 Trojans. Although (20961) Arkesilaos has the diameter only $D = (24 \pm 5)$ km, it is the only asteroid with $H < 12$, for which the associated family has a reasonable number of members N_{memb} even for small values of the cut-off velocity v_{cutoff} (see Section 4.2). As this is also the only larger body located near the centre of the family in the space of proper elements, we treat (20961) Arkesilaos as the largest remnant of the parent body, whose diameter we estimate to be $D_{PB(SPH)} \simeq 87$ km. Given that the mass ratio of the largest remnant and the parent body, as derived from SPH simulations of Durda et al. (2007), is $M_{LR}/M_{PB} \simeq 0.02$ only, it seems this family inevitably originated from a catastrophic disruption.

5.5 Ennomos

In our previous work, we reported a discovery of a possible family associated with asteroid (4709) Ennomos. With new data, we can still confirm that there is a significant cluster near this body, but when we take into account our '$N_{memb}(v_{cutoff})$' criterion described above, it turns out that the family is rather associated with asteroid (17492) Hippasos. It is a relatively numerous group composed of almost 100 bodies, situated near the border of the stable librating zone L_5 at high inclinations, ranging from $I_p \in \langle 26.^\circ 86; 30.^\circ 97\rangle$, and $a_p \in \langle 5.225; 5.338\rangle$ au.

5.6 2001 UV_{209}

Using new data, we discovered a 'new' family around asteroid (247341) 2001 UV_{209}, which is the second and apparently the last observable family in our sample. Similar to the Ennomos family, it is located near the border of the L_5 zone on high inclinations $I_p \in \langle 24.^\circ 02; 26.^\circ 56\rangle$ and $a_p \in \langle 5.218; 5.320\rangle$ au. This family has an exceptionally steep slope of the SFD, with $\gamma = -8.6 \pm 0.9$, which may indicate a recent collisional origin or a disruption at the boundary of the libration zone, which may be indeed size-selective as explained in Chrenko et al. (2015).

Table 2. Derived properties of Trojan families. We list here the family designation, the diameter of the largest remnant D_{LR}, the minimal diameter of the parent body min D_{PB}, obtained as the sum of all observed family members, the diameter of the parent body $D_{PB(SPH)}$ and the mass ratio M_{LR}/M_{PB} of the largest fragment and the parent body, both derived from our fits by scaled SPH simulations performed by Durda et al. (2007). We use this ratio to distinguish between the catastrophic disruption ($M_{LR}/M_{PB} < 0.5$) and the cratering ($M_{LR}/M_{PB} > 0.5$). Finally, there is the escape velocity v_{esc} from the parent body and estimated age of the family derived in this and our previous work (Brož & Rozehnal 2011).

Family designation	D_{LR} (km)	min D_{PB}	$D_{PB(SPH)}$	M_{LR}/M_{PB}	v_{esc} (m s^{-1})	Age (Gyr)	Notes, references
Hektor	250 ± 26	250	257	0.92	73	0.3–3	1, 3
Eurybates	59.4 ± 1.5	100	155	0.06	46	1.0–3.8	2
1996 RJ	58.3 ± 0.9	61	88	0.29	26	–	2, 4
Arkesilaos	24 ± 5	37	87	0.02	16	–	2
Ennomos	55.2 ± 0.9	67–154	95–168	0.04–0.19	29–66	1–2	2, 5
2001 UV$_{209}$	16.3 ± 1.1	32	80	0.01	14	–	2

Notes. [1]D_{LR} derived by Marchis et al. (2014),
[2]D_{LR} derived by Grav et al. (2012),
[3]bilobe, satellite (Marchis et al. 2014),
[4]very compact, Brož & Rozehnal (2011),
[5]D_{PB} strongly influenced by interlopers,
[6]The largest fragment of Ennomos family is (17492) Hippasos.

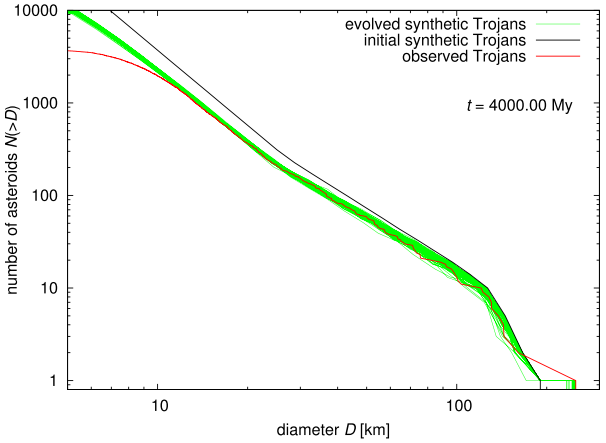

Figure 9. Simulations of the collisional evolution of L_4 Trojans with the Boulder code (Morbidelli et al. 2009). Shown here is the initial cumulative SFD of a synthetic population (black) and the SFD of the observed one (red). Green are the final SFDs of 100 synthetic populations with the same initial SFD but with different random seeds, after 4 Gyr of a collisional evolution. The evolution of bodies larger than $D > 50$ km is very slow, hence we can consider this part of the SFD as captured population.

6 COLLISIONAL MODELS OF THE TROJAN POPULATION

In order to estimate the number of collisional families among L_4 Trojans, we performed a set of 100 simulations of the collisional evolution of Trojans with the Boulder code (Morbidelli et al. 2009) with the same initial conditions, but with different values of the random seed.

6.1 Initial conditions

We set our initial conditions of the simulations such that 4 Gyr of collisional evolution leads to the observed cumulative SFD of L_4 Trojans (red curve in Fig. 9). We constructed the initial synthetic SFD as three power laws with the slopes $\gamma_a = -6.60$ in the size range from $D_1 = 117$ km to $D_{max} = 250$ km, $\gamma_b = -3.05$ from $D_2 = 25$ km to D_1 and $\gamma_c = -3.70$ from $D_{min} = 0.05$ km to D_2. The synthetic initial population was normalized to contain $N_{norm} = 11$ asteroids with diameters $D \geq D_1$.

To calculate the target strength Q_D^*, we used a parametric formula of Benz & Asphaug (1999):

$$Q_D^* = Q_0 R_{PB}^a + B \rho_{bulk} R_{PB}^b, \quad (2)$$

where R_{PB} is the parent body radius in centimetres, ρ_{bulk} its bulk density, which we set to be $\rho_{bulk} = 1.3$ g cm^{-3} for synthetic Trojans (cf. Marchis et al. 2014). As of constants a, b, B and Q_0, we used the values determined by Benz & Asphaug (1999) for ice at the impact velocity $v_{imp} = 3$ km s^{-1}, which are $a = -0.39$, $b = 1.26$, $B = 1.2$ erg cm^3 g^{-2} and $Q_0 = 1.6 \cdot 10^7$ erg g^{-1}.

In our model, we take into account only Trojan versus Trojan collisions, as the Trojan region is practically detached from the main belt. Anyway, main-belt asteroids with eccentricities large enough to reach the Trojan region are usually scattered by Jupiter on a time-scale significantly shorter than the average time needed to collide with a relatively large Trojan asteroid. We thus assumed the values of collisional probability $P_i = 7.80 \cdot 10^{-18}$ km^{-2} yr^{-1} and the impact velocity $v_{imp} = 4.66$ km s^{-1} (Dell'Oro et al. 1998). Unfortunately, Benz & Asphaug (1999) do not provide parameters for ice at the impact velocities $v_{imp} > 3$ km s^{-1}.

We also ran several simulations with appropriate values for basalt at impact velocity $v_{imp} = 5$ km s^{-1} ($a = -0.36$, $b = 1.36$, $B = 0.5$ erg cm^3 g^{-2} and $Q_0 = 9 \cdot 10^7$ erg g^{-1}).

Both models qualitatively exhibit the same evolution of SFD and they give approximately the same total numbers of disruptions and craterings occurred, but for basalt, the model gives three times fewer observable families originated by cratering than for ice. The results for the ice match the observation better, so we will further discuss the results for ice only.

6.2 Long-term collisional evolution

The results of our simulations of the collisional evolution are shown in Fig. 9. Our collisional model shows only little changes above $D > 50$ km over the last 3.85 Gyr (i.e. post-LHB phase only). Slopes of the initial synthetic population and the observed L_4 population differ by $\Delta\gamma < 0.1$ in the size range from 50 to 100 km, while a relative decrease of the number of asteroids after 3.85 Gyr of collisional evolution is only about 12 per cent in the same size

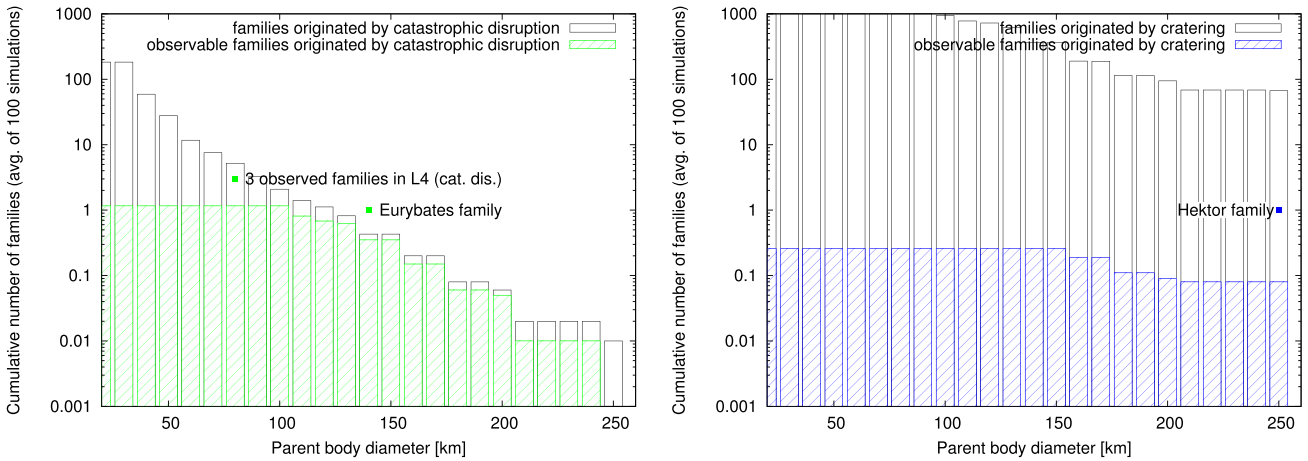

Figure 10. The dependence of the cumulative number (an average over 100 simulations) of catastrophic disruptions among Trojans (left-hand panel) and cratering events (right-hand panel) on the target diameter $D_{\rm PB}$ (black boxes), and a subset of those Trojan families, which should be detected in contemporary observational data, i.e. with the number of fragments $N(D > 10\,{\rm km}) > 10$ (green boxes for disruptions and blue boxes for craterings). In other words, colour boxes represent simulated detections of families based on the expected effectiveness of our detection methods. This is the reason, why the cumulative number of the observable families does not strictly increase with the decreasing parent body size, but is rather constant under the limit of about 95 km in the case of catastrophic disruptions and 145 km in the case of craterings. There are also observed families marked for a comparison. Three of the four observed families in L_4 cloud originated by catastrophic disruption, while only one (Hektor) originated by cratering event (cf. Table 1).

range. Hence, we can consider this part of the Trojan population as a representative sample of the source population, which is not much affected by collisional evolution. Therefore, these Trojans provide very useful information about the source population, from which they were captured (as modelled in Nesvorný et al. 2013).

6.3 An estimate of the number of observable families

From our set of simulations, we also obtained the number of collisions leading to collisional families among L_4 Trojans, namely catastrophic disruptions, where the mass ratio of the largest remnant and the parent body $M_{\rm LR}/M_{\rm PB} < 0.5$, and cratering events, where $M_{\rm LR}/M_{\rm PB} > 0.5$. As one can verify in Fig. 10, these numbers are dependent on the diameter of the parent body $D_{\rm PB}$.

However, not all of these collisions produce families which are in fact observable (detectable). There are generally two possible obstacles in the detection of a family in the space of proper elements: (i) somewhat more concentrated background population, due to which our detection methods (both 'randombox' and HCM, see Chapter 4) may fail, if the number of observed fragments is too low in comparison with the background, and (ii) an observational incompleteness, which means that in the case of Trojans, a substantial part of fragments with sizes $D < 10\,{\rm km}$ is still unknown, what again reduces a chance of a family detection.

For these reasons, we constructed a criterion of observability that a synthetic family must fulfill in order to be detectable in the current conditions (i.e. we simulated a detection of synthetic families by the same methods we used to detect the real ones). The simplest criterion could be that a family must contain at least $N_{\rm min} = 10$ fragments with diameter $D \geq 10\,{\rm km}$.

Within 100 simulations, there were 93 catastrophic disruptions of bodies with diameters $D_{\rm PB} > 100\,{\rm km}$, but only 50 of them produced more than 10 fragments with $D \geq 10\,{\rm km}$, see Fig. 10. Hence, the probability that we would observe a collisional family originated by a catastrophic disruption of a parent body with $D_{\rm PB} > 100\,{\rm km}$ is only 0.50, which matches the observations (namely Eurybates family with $D_{\rm PB(SPH)} \simeq 155$ km, see Table 2). This value is also roughly consistent with our previous estimate based on the stationary model (Brož & Rozehnal 2011), which gives the value 0.32 with new observational data.

As one can also see in Fig. 10, the number of cratering events is about one to two orders higher than the number of catastrophic disruptions, however, they do not produce enough fragments larger than $D \geq 10\,{\rm km}$. For the parent body size $D_{\rm PB} > 100\,{\rm km}$, there occurred almost 45 000 cratering events within 100 simulations which produced the largest fragment with $D_{\rm LF} \geq 1\,{\rm km}$, but only 10 of them fulfill our criterion of observability. Hence, the probability that we can observe a family originated by a cratering of a parent body with $D_{\rm PB} > 100\,{\rm km}$ is only 0.10, at least with contemporary data. From a statistical point of view, this can actually correspond to the Hektor family.

As we have already demonstrated in Brož & Rozehnal (2011), the number of families is not significantly affected by chaotic diffusion or by a ballistic transport outside the libration zone.

7 SPH SIMULATIONS OF HEKTOR FAMILY

As we have already mentioned in Section 5.2, (624) Hektor is very interesting Trojan asteroid with possibly bilobed shape and a small moon. Diameters of (624) Hektor stated in Marchis et al. (2014) are as follows: equivalent diameter $D_{\rm eq} = (250 \pm 26)$ km for a convex model, the individual diameters of the lobes $D_{\rm A} = (220 \pm 22)$ km, $D_{\rm B} = (183 \pm 18)$ km for a bilobed version. Estimated parameters of the moon are: the diameter $D_{\rm m} = (12 \pm 3)$ km, the semimajor axis $a_{\rm m} = (623 \pm 10)$ km, the eccentricity $e_{\rm m} = (0.31 \pm 0.03)$ and the inclination (with respect to the primary equator) $I_{\rm m} = (50 \pm 1)^\circ$.

As we associate (624) Hektor with the collisional family, we would like to know, how the properties of the family are influenced by the shape of target body. We therefore performed a series of SPH simulations aiming to explain the origin of the Hektor family, for both cases of convex and bilobed shape of its parent body.

7.1 Methods and initial conditions

We simulated a collisional disruption using the SPH code SPH5 (Benz & Asphaug 1994). We performed two sets of simulations. In

Table 3. Material constants used in our SPH simulations for basalt and silicated ice (30 per cent of silicates). Listed here are: the zero-pressure density ρ_0, bulk modulus A, non-linear compressive term B, sublimation energy E_0, Tillotson parameters a, b, α and β, specific energy of incipient vaporization $E_{\rm iv}$, complete vaporization $E_{\rm cv}$, shear modulus μ, plastic yielding Y, melt energy $E_{\rm melt}$ and Weibull fracture parameters k and m. Values we used for silicated ice are identical to those of pure ice, except density ρ_0, bulk modulus A and Weibull parameters k and m. All values were adopted from Benz & Asphaug (1999).

Quantity	Basalt	Silicated ice	Unit
ρ_0	2.7	1.1	g cm^{-3}
A	$2.67 \cdot 10^{11}$	$8.44 \cdot 10^{10}$	erg cm^{-3}
B	$2.67 \cdot 10^{11}$	$1.33 \cdot 10^{11}$	erg cm^{-3}
E_0	$4.87 \cdot 10^{12}$	$1.00 \cdot 10^{11}$	erg g^{-1}
a	0.5	0.3	–
b	1.5	0.1	–
α	5.0	10.0	–
β	5.0	5.0	–
$E_{\rm iv}$	$4.72 \cdot 10^{10}$	$7.73 \cdot 10^{9}$	erg g^{-1}
$E_{\rm cv}$	$1.82 \cdot 10^{11}$	$3.04 \cdot 10^{10}$	erg g^{-1}
μ	$2.27 \cdot 10^{11}$	$2.80 \cdot 10^{10}$	erg cm^{-3}
Y	$3.5 \cdot 10^{10}$	$1.0 \cdot 10^{10}$	erg g^{-1}
$E_{\rm melt}$	$3.4 \cdot 10^{10}$	$7.0 \cdot 10^{9}$	erg g^{-1}
k	$4.0 \cdot 10^{29}$	$5.6 \cdot 10^{38}$	cm^{-3}
m	9.0	9.4	–

the first one, we simulated an impact on a single spherical asteroid. In the second, on a bilobed asteroid represented by two spheres positioned next to each other. The two touching spheres have a narrow interface, so that the SPH quantities do not easily propagate between them. In this setup, we are likely to see differences between sinlge/bilobed cases as clearly as possible.

As for the main input parameters (target/impactor sizes, the impact velocity and the impact angle), we took the parameters of our best-fitting SFDs, obtained by Durda et al. (2007) scaling method, see Section 5.2.2 and Fig. 8.

To simulate a collision between the parent body and the impactor, we performed a limited set of simulations: (i) a single spherical basalt target with diameter $D_{\rm PB} = 260$ km versus a basalt impactor with diameter $D_{\rm imp} = 48$ km; (ii) the single basalt target $D_{\rm PB} = 260$ km versus an ice impactor (a mixture of ice and 30 per cent of silicates) with $D_{\rm imp} = 64$ km (impactor diameter was scaled to get the same kinetic energy); (iii) a bilobed basalt target approximated by two spheres with diameters $D_{\rm PB} = 200$ km each (the total mass is approximately the same) versus a basalt impactor with $D_{\rm imp} = 48$ km; (iv) a single spherical ice target $D_{\rm PB} = 260$ km versus an ice impactor $D_{\rm imp} = 38$ km (impactor diameter was scaled to get the same ratio of the specific kinetic energy Q to the target strength $Q^*_{\rm D}$).

The integration was controlled by the Courant number $C = 1.0$, a typical timestep thus was $\Delta t \simeq 10^{-5}$ s, and the timespan was $t_{\rm stop} = 100$ s. The Courant condition was the same in different materials, using always the maximum sound speed $c_{\rm s}$ among all SPH particles, as usually.

We used $N_{\rm SPH,st} = 10^5$ SPH particles for the single spherical target and $N_{\rm SPH,\,bt} = 2 \cdot 10^5$ for the bilobed one. For impactor $N_{\rm SPH,\,i} = 10^3$ SPH particles. We assumed the Tillotson equation of state (Tillotson 1962) and material properties, which are listed in Table 3.

We terminated SPH simulations after 100 s from the impact. This time interval is needed to establish a velocity field of fragments and to complete the fragmentation. Then we handed the output of

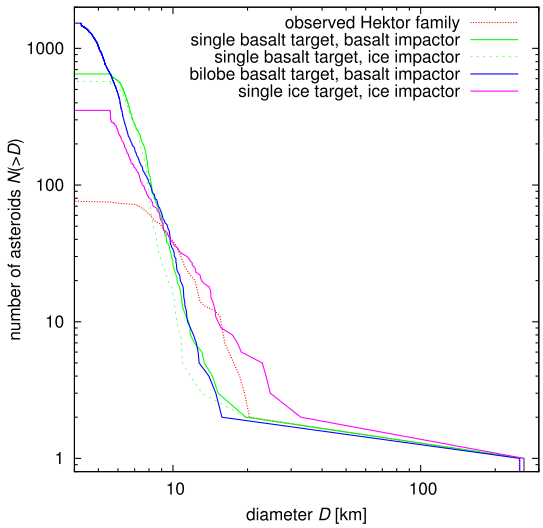

Figure 11. A comparison of size–frequency distributions of the observed Hektor family (red dotted) and SFDs of synthetic families created by different SPH simulations, always assuming the impactor velocity $v_{\rm imp} = 4$ km s^{-1} and the impact angle $\varphi_{\rm imp} = 60°$. For a single spherical target (green lines), we assumed the diameter $D_{\rm PB} = 260$ km; for a bilobe target (blue line), we approximated the lobes as spheres with diameters $D_{\rm PB} = 200$ km each. The impactor size was assumed to be $D_{\rm imp} = 48$ km in the case of basalt, $D_{\rm imp} = 64$ km in the case of silicate ice impacting on basalt target (scaled to the same $E_{\rm imp}$) and $D_{\rm imp} = 38$ km in the case of silicate ice impacting on ice target (scaled to the same $Q/Q^*_{\rm D}$). Fragments of the impactor were purposely removed from this plot, as they do not remain in the libration zone for our particular impact orbital geometry.

the SPH simulation as initial conditions to the N-body gravitational code Pkdgrav (Richardson et al. 2000), a parallel tree code used to simulate a gravitational re-accumulation of fragments. Unlike Durda et al. (2007), who calculated radii of fragments R from the smoothing length h as $R = h/3$, we calculated fragments radii from their masses m and densities ρ as $R = (m/(4\pi\rho))^{1/3}$.

We ran Pkdgrav with the timestep $\Delta t = 5.0$ s and we terminated this simulation after $t_{\rm evol} = 3$ d of evolution. To ensure this is sufficiently long, we also ran several simulations with $t_{\rm evol} = 5$ d, but we had seen no significant differences between final results.

We used the nominal value for the tree opening angle, $\mathrm{d}\theta = 0.5$ rad, even though for the evolution of eventual moons, it would be worth to use even smaller value, e.g. $\mathrm{d}\theta = 0.2$ rad.

7.2 Resulting SFDs

From the output of our simulations, we constructed SFDs of synthetic families, which we compare to the observed one, as demonstrated in Fig. 11. As one can see, there are only minor differences between SFDs of families created by the impacts on the single and bilobed target, except the number of fragments with diameter $D < 5$ km, but this is mostly due to different numbers of SPH particles. However, there are differences between ice and basalt targets. Basalt targets provide generally steeper SFDs with smaller largest remnants than the ice target.

To make the comparison of these synthetic initial SFDs to each other more realistic, we removed the fragments of the impactor from our synthetic families. This is because fragments of the impactor often do not remain in the libration zone. Note that this procedure does not substitute for a full simulation of further evolution; it serves just for a quick comparison of the SFDs.

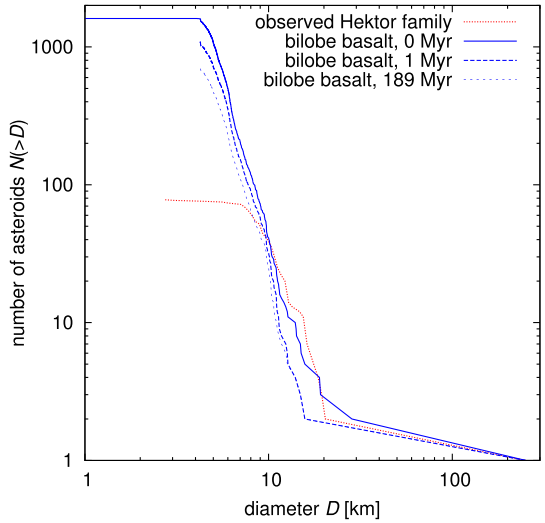

Figure 12. A simulation of evolution of the SFD of a synthetic Hektor family due to a ballistic transport and chaotic diffusion. One can see here a rapid change of SFD within the first 1 Myr after the breakup as the fragments of the impactor leaved the libration zone in our impact geometry. This ballistic transport resulted in a reduction of the number of particularly larger bodies in our case. Further evolution due to the chaotic diffusion seems to cause the reduction of mostly smaller bodies. Note that the initial SFD (0 Myr) contains some fragments of the impactor, so the blue solid curve looks different than the curve in Fig. 11, where the fragments of the impactor were removed.

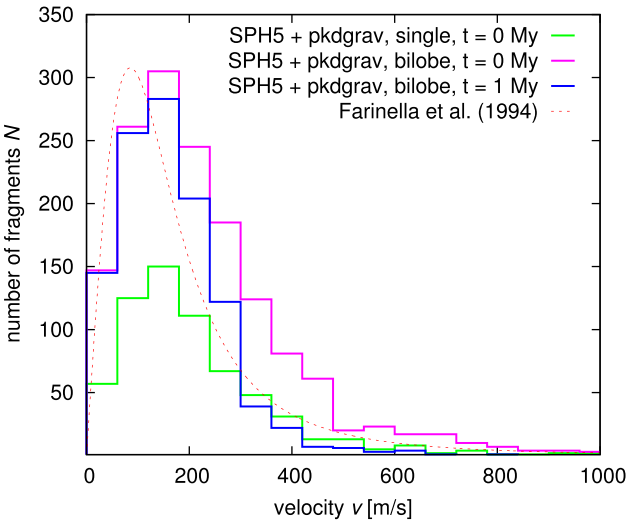

Figure 13. Velocity distributions of fragments originated in various SPH simulations (green, violet) in comparison with the model of Farinella et al. (1994) we used in our *N*-body simulations of isotropic disruption and dynamical evolution (see Section 5.2.1). Shown here is also the distribution of velocities after 1 Myr of evolution, i.e. of fragments that remained in libration zones.

To match the observed SFD of the Hektor family more accurately, we should perform a much larger set of simulations with different sizes of projectiles and also different compositions (mixtures of ice and basalt). However, material parameters of these mixtures are generally not known. Regarding the material constants of pure ice, we have them for the impact velocity $v_{\rm imp} = 3\,{\rm km\,s^{-1}}$ only (Benz & Asphaug 1999). There are also some differences between SFDs of single and bilobe targets, so we should perform these simulations for each target geometry. However, we postpone these detailed simulations for future work; in this work, we further analyse results of simulations with basalt targets and we focus on the evolution of the SFDs.

It should be emphasized that the SFDs presented here correspond to very young synthetic families, hence they are not affected by any dynamical and collisional evolution yet. To reveal possible trends of the evolution by a ballistic transport and chaotic diffusion, we prepared initial conditions for the SWIFT integrator, similarly as described in Section 5.2.1, let the simulation run and monitored the corresponding evolution of the SFD. The results can be seen in Fig. 12. The biggest difference between $t = 0$ and 1 Myr is caused by a ballistic transport outside the libration zone – fragments (especially of the impactor) missing from the SFD at $t = 1$ Myr were perturbed too much to remain in the libration zone, at least for a given impact geometry. We actually tested two impact geometries: in the direction tangential and perpendicular to the orbit.

This may be important for the method we used in Section 5.2.2 to derive a preliminary parent body size and other properties of the family. The SFDs obtained by Durda et al. (2007) were directly compared in their work to the main-belt families, however, there is a part of fragments among Trojans (in our case even the largest ones, see Fig. 12), which cannot be seen in the space of resonant elements, because they do not belong to Trojans any more. Fortunately, values of pseudo-χ^2 we computed in Section 5.2.2 depend rather weakly on the distribution of a few largest bodies. Even so, we plan to analyse SFDs of synthetic families more carefully in future works.

7.3 Resulting velocity fields

In our *N*-body simulations, we used the model of isotropic disruption (Farinella et al. 1994). As we compared the synthetic family with the observed one (see Section 5.2.1), we simulated only the evolution of bodies with relatively low-ejection velocities ($v < 200\,{\rm m\,s^{-1}}$), because the observed family is confined by the cut-off velocity $v_{\rm cutoff} = 110\,{\rm m\,s^{-1}}$. Very small fragments with higher velocities may be still hidden in the background.

Here, we compare Farinella's model to the velocity fields of fragments from SPH simulations, see Fig. 13. We realized that Farinella's model is not offset substantially with respect to other velocity histograms, especially at lower velocities, $v < 200\,{\rm m\,s^{-1}}$. On the other side, there remained some fragments of the impactor with velocities $v > 2\,{\rm km\,s^{-1}}$ in our SPH simulations, which are not produced in the isotropic model. It does not affect a comparison of the synthetic and observed families in the space of proper elements, as these high-velocity fragments leaved the Trojan region in our case, but it does affect the SFD of the synthetic family. As a consequence, one should always analyse SFDs and velocity fields together.

We also simulated a further evolution of the velocity field. After just 1 Myr of evolution, there remained no bodies with $v > 1.5\,{\rm km\,s^{-1}}$ in our impact geometries, and as one can see in Fig. 13, there was a rapid decrease in the number of fragments with initial $v > 300\,{\rm m\,s^{-1}}$. The resulting histogram is again similar to that of the simple isotropic model.

7.4 Synthetic moons

In our simulation of the impact of basalt projectile on the bilobe-shape basalt target, we spotted two low-velocity fragments with original velocities 130 and $125\,{\rm m\,s^{-1}}$, which were consequently

Table 4. A comparison of the sizes and the orbital parameters (i.e. semi-major axis a, eccentricity e and period P) of the observed moon of (624) Hektor as listed in Marchis et al. (2014), with the parameters of synthetic moons SPH I and SPH II captured in our SPH simulation of impact on the bilobed target.

Desig.	Diam. (km)	a (km)	e	P (d)
Observed	12 ± 3	623.5 ± 10	0.31 ± 0.03	2.9651 ± 0.0003
SPH I	2.2	715	0.82	1.2
SPH II	2.7	370	0.64	0.4

captured as moons of the largest remnant. Their sizes and orbital parameters are listed in Table 4.

These satellites were captured on orbits with high eccentricities ($e = 0.82$ and 0.64, respectively), which are much higher than the eccentricity of the observed moon determined by Marchis et al. (2014) ($e = 0.31 \pm 0.03$). However, this could be partly caused by the fact, that we handed the output of (gravity-free) SPH simulations to the gravitational N-body code after first 100 s. Hence, fragments leaving the parent body could move freely without slowing down by gravity. More importantly, we do not account for any long-term dynamical evolution of the moons (e.g. by tides or binary YORP).

When compared to the observed satellite, the diameters of the synthetic moons are several times smaller. This is not too surprising, given that the results for satellite formation are at the small end of what can be estimated with our techniques (median smoothing length $h = 2.3$ km; satellite radius $r \simeq 1.2$ km). The size of captured fragments could also be dependent on impact conditions as different impact angles, impactor velocities and sizes (as is the case for scenarios of Moon formation) which we will analyse in detail in the future and study with more focused simulations.

8 CONCLUSIONS

In this paper, we updated the list of Trojans and their proper elements, what allowed us to update parameters of Trojan families and to discover a new one (namely 2001 UV_{209} in L_5 population). We focused on the Hektor family, which seems the most interesting due to the bilobed shape of the largest remnant with a small moon and also its D-type taxonomical classification, which is unique among the collisional families observed so far.

At the current stage of knowledge, it seems to us there are no major inconsistencies among the observed number of Trojan families and their dynamical and collisional evolution, at least in the current environment.

As usual, we 'desperately' need new observational data, namely in the size range from 5 to 10 km, which would enable us to constrain the ages of asteroid families on the basis of collisional modelling and to decide between two proposed ages of Hektor family, 1–4 Gyr or 0.1–2.5 Gyr.

As expected, there are qualitative differences in impacts on single and bilobed targets. In our setup, the shockwave does not propagate easily into the secondary, so that only one half the mass is totally damaged as one can see in Fig. 14. On the other hand, the resulting SFDs are not that different, as we would expect.

Even so, there is a large parameter space, which is still not investigated (i.e. the impact geometry with respect to the secondary, secondary impacts, the position in the orbit). SPH simulations of impacts on bilobed or binary targets thus seem very worthy for future research.

Our work is also a strong motivation for research of disruptions of weak bodies (e.g. comets), better understanding the cometary disruption scaling law and also for experimental determination of material constants, which appear in the respective equation of state.

As a curiosity, we can also think of searching for the remaining projectile, which could be still present among Trojans on a trajectory substantially different from that of family. A substantial part of projectile momentum is preserved in our simulations, so we may turn the logic and we may assume the projectile most likely came from the Trojan region and then it should remain in this region too.

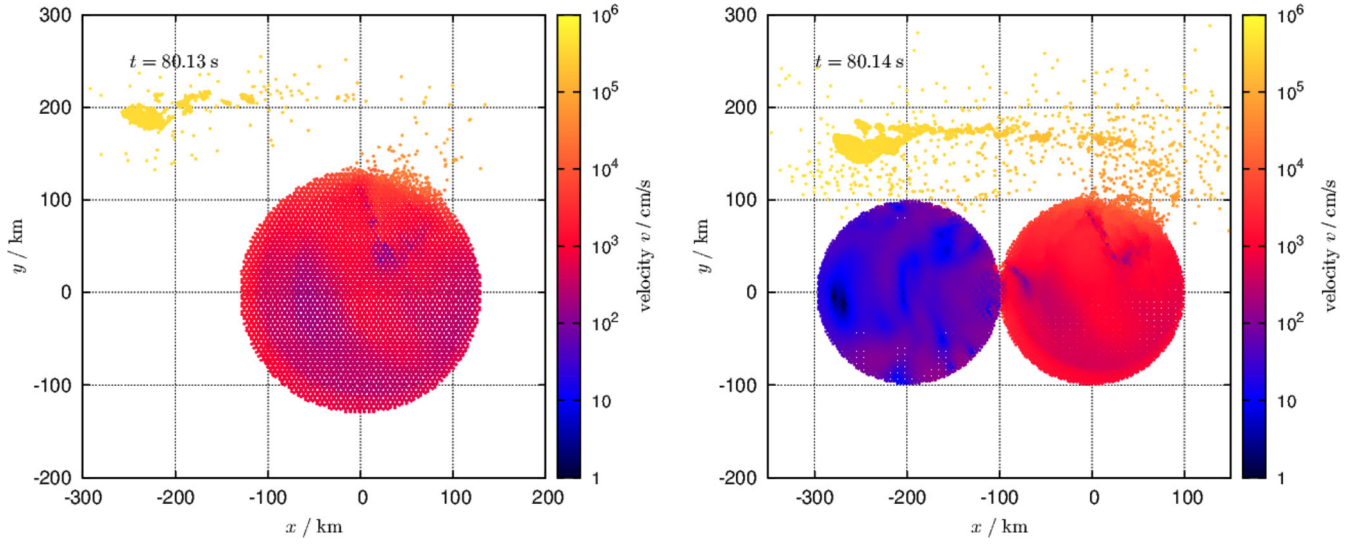

Figure 14. A comparison of SPH simulations of a disruption of a single body (basalt) with diameter $D_{\rm target} = 250$ km, by an impactor with the diameter $D_{\rm imp} = 48$ km (silicate ice) (left) and a disruption of a bilobe basalt target, with $D_{\rm target} = 198$ km for each sphere, by an impactor with $D_{\rm imp} = 46$ km (silicate ice) (right). Time elapsed is $t = 80.1$ s in both cases. There are notable physical differences between the two simulations, especially in the propagation of the shock wave, which is reflected from free surfaces, the number of secondary impacts, or the fragmentation (damage) of the target. Nevertheless, the amount of ejected material and the resulting size–frequency distributions do not differ that much (cf. Fig. 11).

ACKNOWLEDGEMENTS

We thank Alessandro Morbidelli for his review which helped to improve the final version of the paper.

The work of MB was supported by the grant no. P209/13/01308S and that of JR by P209/15/04816S of the Czech Science Foundation (GA CR). We acknowledge the usage of computers of the Stefanik Observatory, Prague.

REFERENCES

Benz W., Asphaug E., 1999, Icarus, 142, 5
Bowell E., Virtanen J., Muinonen K., Boattini A., 2002, in Bottke W. F., Jr, Cellino A., Paolicchi P., Binzel R. P., eds, Asteroids III. Univ. Arizona Press, Tucson, p. 27
Brož M., Morbidelli A., 2013, Icarus, 223, 844
Brož M., Rozehnal J., 2011, MNRAS, 414, 565
Brož M. et al., 2013, AAP, 551, A117
Carruba V., Nesvorný D., 2016, MNRAS, 457, 1332
Chrenko O., Brož M., Nesvorný D., Tsiganis K., Skoulidou D. K., 2015, MNRAS, 451, 2399
Cruikshank D. P., Dalle Ore C. M., Roush T. L., Geballe T. R., Owen T. C., de Bergh C., Cash M. D., Hartmann W. K., 2001, Icarus, 153, 348
Dell'Oro A., Marzari F., Paolicchi P., Dotto E., Vanzani V., 1998, A&A, 339, 272
Dohnanyi J. S., 1969, J. Geophys Res., 74, 2531
Durda D. D., Bottke W. F., Nesvorný D., Enke B. L., Merline W. J., Asphaug E., Richardson D. C., 2007, Icarus, 186, 498
Emery J. P., Cruikshank D. P., Van Cleve J., 2006, Icarus, 182, 496
Emery J. P., Burr D. M., Cruikshank D. P., 2011, AJ, 114, 25
Farinella P., Froeschlé C., Gonczi R., 1994, in Milani A., Di Martino M., Cellino A., eds., Asteroids, Comets, Meteors 1993. Kluwer Academic Publishers, Dordrecht, p. 205
Goldreich P., Lithwick Y., Sari R., 2004, ApJ, 614, 497
Grav T. et al., 2011, ApJ, 742, 40
Grav T., Mainzer A. K., Bauer J., Masiero J. R., Nugent C. R., 2012, ApJ, 759, 49
Ivezić Z., Jurić M., Lupton R. H., Tabachnik S., Quinn T., 2002, in Tyson J. A., Wolff S., eds, Proc. SPIE Conf. Ser. Vol. 4836, Survey and Other Telescope Technologies and Discoveries. Kluwer, Dordrecht, p. 98
Laskar J., Robutel P., 2001, Celest. Mech. Dyn. Astron., 80, 39
Levison H. F., Duncan M., 1994, Icarus, 108, 18
Levison H. F., Bottke W. F., Gounelle M., Morbidelli A., Nesvorný D., Tsiganis K., 2009, Nature, 460, 364
Lyra W., Johansen A., Klahr H., Piskunov N., 2009, A&A, 493, 1125
Mainzer A. et al., 2011, ApJ, 741, 90
Marchis F. et al., 2014, ApJ, 783, L37
Morbidelli A., Levison H. F., Tsiganis K., Gomes R., 2005, Nature, 435, 462
Morbidelli A., Bottke W. F., Nesvorný D., Levison H. F., 2009, Icarus, 204, 558
Morbidelli A., Brasser R., Gomes R., Levison H. F., Tsiganis K., 2010, AJ, 140, 1391
Nesvorný D., Vokrouhlický D., Morbidelli A., 2013, ApJ, 768, 45
Nesvorný D., Brož M., Carruba V., 2015, in Michel P., DeMeo F. E., Bottke W. F., eds, Asteroids IV. Arizona Univ. Press, Tucson, p. 297
Richardson D. C., Quinn T., Stadel J., Lake G., 2000, Icarus, 143, 45
Tillotson E, 1962, Nature, 195, 763
Usui F. et al., 2011, PASJ, 63, 1117
Vinogradova T. A., 2015, MNRAS, 454, 2436
Zappalà V., Cellino A., Farinella P., Milani A., 1994, AJ, 107, 772

This paper has been typeset from a TEX/LATEX file prepared by the author.